Monthly Notices of the ROYAL ASTRONOMICAL SOCIETY

MNRAS **538,** 1906–1920 (2025) https://doi.org/10.1093/mnras/staf338
Advance Access publication 2025 February 26

Infrared spectroscopy of astrophysical ice analogues at oblique angles

C. González Díaz ,★ H. Carrascosa and G. M. Muñoz Caro
Centro de Astrobiología (CSIC-INTA), Ctra. de Ajalvir, km 4, Torrejón de Ardoz, E-28850 Madrid, Spain

Accepted 2025 February 19. Received 2025 February 6; in original form 2024 July 17

ABSTRACT

In astrochemical exploration, infrared (IR) spectroscopy is vital for understanding the composition and structure of ice in various space environments. This article explores the impact of incident angles on IR spectroscopy, focusing on molecular components present in interstellar and circumstellar ice mantles such as CO, CO_2, H_2O, CH_3OH, NH_3, CH_4, H_2S. The experiment involves changing the angle at which the IR beam hits the surface used for ice deposition. It is important to measure the density of the ice layer accurately, especially for experiments that involve using different angles in IR spectroscopy. Furthermore, the experimental methodology allowed us to derive the *effective* refraction index values in the IR range for each ice component. Existing corrections typically consider geometric configurations but overlook the refractive index of the ice (n), a factor dependent on ice composition. The study reveals that the incident angle and the refractive index, determine the path length of the IR beam across the ice sample. This insight challenges conventional corrections, impacting the integrated absorption values of the IR bands and column densities. In addition, for certain ice components, variations in the incidence angle affect the longitudinal (LO) and transverse (TO) optical modes of the ice, leading to observable changes in the IR band profiles that provide information on the amorphous or crystalline structure of the ice. The practical implications of this work apply to experimental setups where normal IR measurements are unfeasible. Researchers using, for example, the standard 45° angle for IR spectroscopy, will benefit from a more accurate estimation of ice column density.

Key words: astrochemistry – radiation mechanisms: non-thermal – methods: laboratory: solid state – techniques: spectroscopic – ISM: molecules – infrared: ISM.

1 INTRODUCTION

In the astrochemical literature, numerous experimental works were devoted to ice infrared (IR) spectroscopy for *in situ* characterization of the ice structure and monitoring of ice processes during irradiation with UV or X-rays, ion bombardment or controlled warm-up. A clear advantage of IR spectroscopy is the comparison to observed spectra of ice in Solar system objects in reflectance, or ice mantles in the coldest regions of interstellar clouds and protoplanetary discs observed in absorbance. In the later observations, the column density of the more abundant ice components along the line of sight can be determined. This revealed an ice mantle composition dominated by water and other simple molecules that include CO, CO_2, CH_3OH, OCN^-, OCS, H_2CO, HCOOH, CH_4, and NH_3, or $NH4^+$, e.g. Öberg, Facchini & Anderson (2023).

The present paper aims to study the IR spectroscopy of common molecular components in interstellar and circumstellar ice mantles, these are CO, CO_2, H_2O, CH_3OH, NH_3, CH_4, and H_2S at different angles of incidence of the IR beam with respect to the substrate used for ice deposition in our experiments. This incident angle determines the path length of the ice intersected by the IR beam, which corresponds to integrated absorption values and column densities larger than the ones measured at normal incidence angle. An application of this work is therefore the correct estimation of the column density in experiments using different incident angles for IR spectroscopy. The objective is to provide a value of the column density that corresponds to the one obtained at normal incident angle, because such value is directly related to the thickness of the ice if porosity is discarded. Typically, the corrections reported in the literature only account for the trivial geometrical configuration of the system, i.e. $N_0 = N_\alpha \cos(\alpha)$ where N_0 is the ice column density measured at normal incidence of the IR beam and N_α the one measured at incident angle α. These works do not take the refractive index of the ice, n, into consideration, which depends mainly on the ice composition, and together with the incident angle, determines the path length of the IR beam across the ice sample. The IR absorbance of a thin sample measured at normal incidence with a linearly polarized beam has been studied in detail by Itoh, Kasuya & Hasegawa (2009).

Transmission IR spectroscopy of thin ice films, performed at incident angle normal to the substrate, allows to observe the vibrations taking place in the plane of the substrate or with vector components in that plane. For other incident angles, the IR beam may interfere with both the surface-parallel and surface-perpendicular vibrational modes. Therefore, even for unpolarized IR beam spectroscopy, which is the technique most commonly used in ice studies, the incident angle can influence the value of the integrated absorption, and also the band profiles to some degree, since these parameters depend on the vibrations activated with IR light. For instance, the so-called longitudinal (LO) and transverse (TO) optical modes of CO ice fall near 2142 and 2138 cm^{-1} (e.g. Palumbo 2006). Unpolarized IR light

★ E-mail: cgondia@inta.es

© 2025 The Author(s).
Published by Oxford University Press on behalf of Royal Astronomical Society. This is an Open Access article distributed under the terms of the Creative Commons Attribution License (https://creativecommons.org/licenses/by/4.0/), which permits unrestricted reuse, distribution, and reproduction in any medium, provided the original work is properly cited.

Downloaded from https://academic.oup.com/mnras/article/538/3/1906/8043270 by guest on 21 April 2026

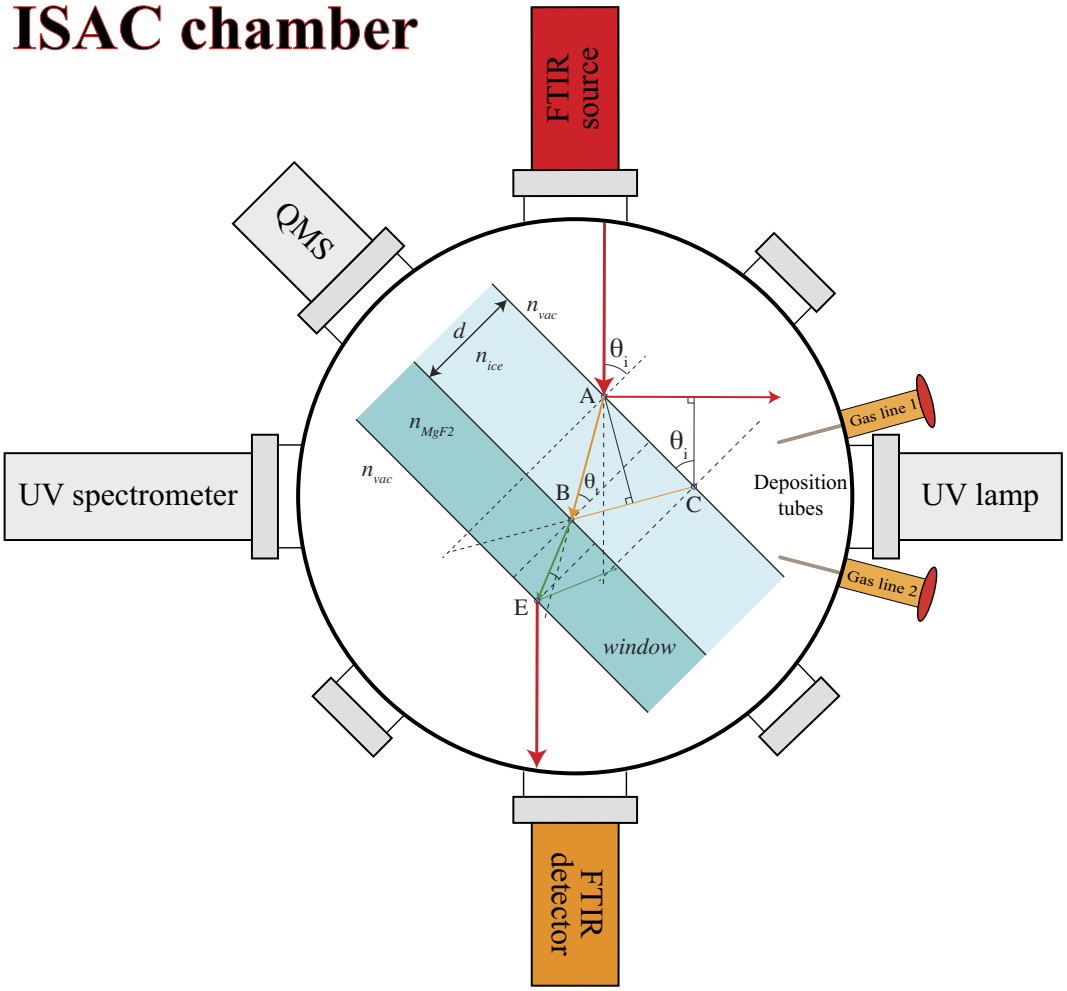


Figure 1. Sketch of the path followed by the IR beam as a function of the incident angle. The positions of the detectors are shown. QMS stands for quadrupole mass spectrometer, FTIR is the Fourier transform IR spectrometer. The FTIR spectrometer with the IR source is facing one viewport and the FTIR detector is on the opposite side. The UV spectrometer is located at the opposite side of the ice sample.

at normal incidence has electric field components parallel to the film surface, and is therefore only sensitive to the TO mode. On the other hand, at oblique angles both the LO and TO modes can be observed. Such LO–TO splitting is attributed to dipole–dipole interactions in CO ice (Zumofen 1978; Lasne et al. 2015), it is most evident in crystalline ice samples but may also be seen in at least partially disordered ice (Muñoz Caro et al. 2016 and references therein).

As discussed above, IR spectroscopy of ices at oblique incidence is used to infer more information from the ice structure, or simply because either the configuration of the vacuum chamber or the experimental protocol do not allow IR spectroscopy at normal incidence. This work presents a methodical study of the effects of incident angle on ice spectroscopy with unpolarized IR light. For this, different incident angles of the IR beam with respect to the ice substrate were explored in the reported experiments.

2 EXPERIMENTAL

2.1 Experimental setup

Experiments were conducted using the Interstellar Astrochemistry Chamber (ISAC), which is an ultrahigh vacuum chamber designed to simulate the conditions present in the interstellar medium (ISM), such as temperature, low particle density, and ultraviolet (UV) radiation field. The base pressure of ISAC is 4×10^{-11} mbar. Further details about ISAC can be found in Muñoz Caro et al. (2010).

The cold finger of the chamber is cooled down using a closed-cycle He cryostat to a temperature close to 8 K, where a sample holder with a MgF_2 window acts as the substrate for ice deposition. However, in the experiments reported in this work, the lowest achievable temperature was 11 K because the radiation shield surrounding the sample holder was removed during these experiments, allowing IR measurements at a wider range of angles. The temperature of the ice sample was measured by placing a silicon diode sensor just below the ice sample and attaching it to the sample holder. The temperature is controlled by a Lakeshore 331 temperature controller with a precision of 0.1 K. For these experiments, the temperature remained constant at 11 K. The gas line system in ISAC allows the introduction of gas species with a controlled composition, monitored by Quadrupole Mass Spectrometry (QMS, Pfeiffer Vacuum, Prisma QMS 200). In the main chamber of ISAC, pressure was monitored using a Bayard–Alpert gauge located approximately 23 cm below the deposition plane. The experimental parameters were recorded during the experiments to ensure constant conditions.

Downloaded from https://academic.oup.com/mnras/article/538/3/1906/8043270 by guest on 21 April 2026

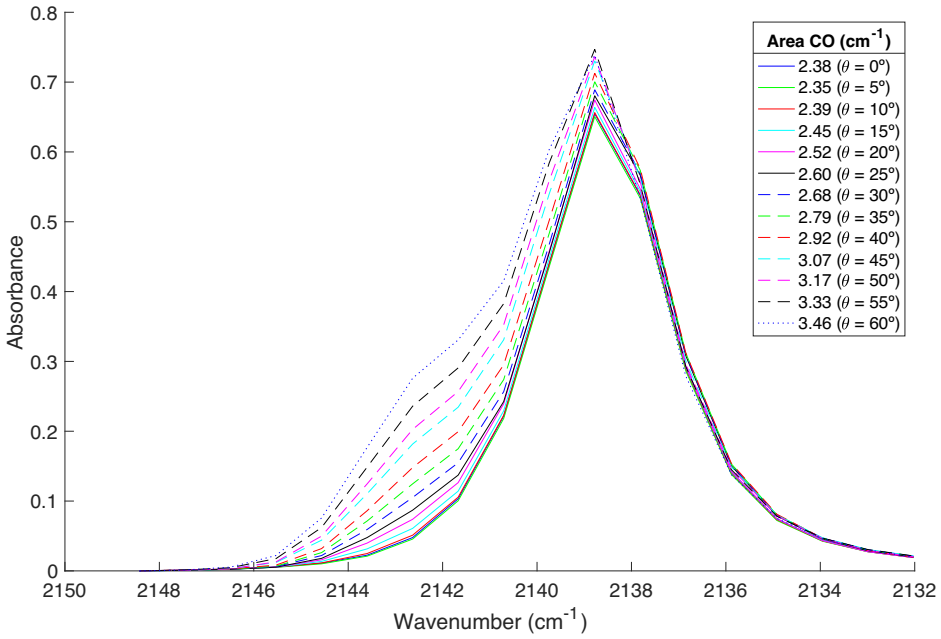


Figure 2. IR spectra of CO ice deposited at 11 K as a function of the incidence angle used for IR spectrometry.

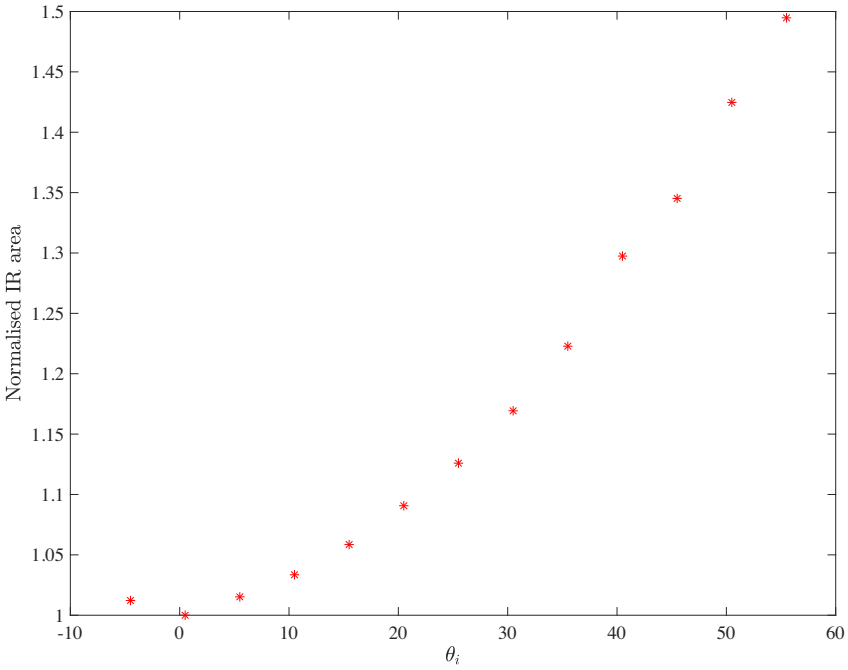


Figure 3. Normalized values of the integrated IR absorption spectra, corresponding to the IR band areas of CO ice deposited at 11 K as a function of the incident angle θ_i.

Fig. 1 shows a scheme of the ISAC set-up. During deposition, the gas valve is opened and the gas is directed to the cold substrate via a deposition tube. The end of this tube is about 3 cm from the substrate, and the sample holder can be rotated at any desired angle using a motorized system. The following abundant molecular components of interstellar and circumstellar ice mantles were introduced into the main chamber for 10 min: CO, CO_2, H_2O, CH_3OH, NH_3, CH_4, and H_2S (one pure component in each experiment). This was achieved by opening the gas line 2 leak valve, see Fig. 1, to attain the desired deposition pressure of 2×10^{-7} mbar.

In these experiments, the angle of deposition with respect to the cold substrate was consistently set at $\theta_i = 0°$. This ensured a perpendicular incidence of the deposited molecules on to the substrate surface, allowing for uniform and controlled ice deposition (González Díaz et al. 2019). After the completion of the deposition of the aforementioned molecular ice components, IR spectra were recorded using Fourier-transform IR spectroscopy (FTIR) in transmittance mode, employing a Bruker Vertex 70 spectrometer operating at a working spectral resolution of 2 cm^{-1}. These spectra

Downloaded from https://academic.oup.com/mnras/article/538/3/1906/8043270 by guest on 21 April 2026

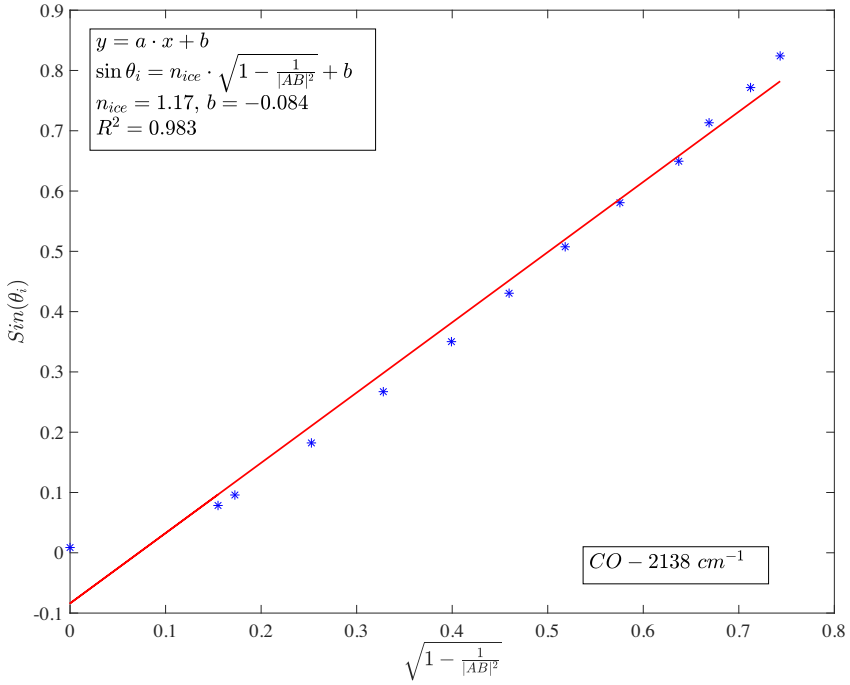


Figure 4. Representation of sine of incident angle of the IR beam, $\sin\theta_i$, for CO ice deposited at 11 K as a function of $\sqrt{1 - \frac{d^2}{|AB|^2}}$. The red-solid trace is the linear fit.

Table 1. Summary of the *effective* index of refraction $n_{\rm ice}$, R-square values of the linear fit applied to obtain $n_{\rm ice}$ as the slope of this fit, and the correction factor $\sqrt{1 - \frac{\sin^2\theta_i}{n_{\rm ice}^2}}$ in equation (6) for $\theta_i = 45°$. The values in this table belong to various bands for different ice compositions. In addition to this correction factor that is dependent on the incident angle θ_i used for IR spectroscopy, the column density value at normal incidence, N_0, is also dependent on the integrated absorbance of the IR band that leads to N_{θ_i} in equation (6). Note that the values of the correction factor obtained at 45° differ significantly from the simple geometric correction factor, i.e. cos(45°) = 0.7071, represented by the dotted green line in Fig. 23, showing the error introduced in the ice column density estimation of previous works that merely relied on this 0.7071 factor.

Ice molecule	λ (cm^{-1})	Index of Refraction	R-Square	Correction factor (45°)
CO	2138	1.17	0.983	0.797
CO_2	2282	1.25	0.940	0.825
	2364	1.47	0.853	0.88
	3708	1.13	0.925	0.877
H_2O	3283	1.00	0.974	0.707
CH_3OH	1020	1.11	0.981	0.771
	2830	1.13	0.994	0.780
	3290	1.06	0.993	0.745
NH_3	1082	1.06	0.913	0.745
	3375	1.56	0.919	0.891
CH_4	1300	1.16	0.981	0.793
	3100	1.13	0.991	0.780
H_2S	2550	1.56	0.969	0.891

were collected at different angles of incidence from 0 to 60°, the latter is the maximum oblique angle allowed in ISAC for IR spectroscopy.

2.2 Column density estimation versus incident angle of the IR beam

Fig. 1 represents the path of the IR beam that passes through the deposited ice, red trace, starting from point A and ending at point E. The substrate used for ice deposition is a MgF_2 window, which has minimal absorption in the mid-IR range displayed in the reported experiments. The line segment $|AB|$ corresponds therefore to the distance travelled by the IR beam through the ice layer. This distance is crucial in determining the absorption and the column density of the IR beam, depending on the incident angle.

From the triangle formed by ABC it follows that

$$|AB| = |BC| = \frac{d}{\cos\theta_t}. \quad (1)$$

Downloaded from https://academic.oup.com/mnras/article/538/3/1906/8043270 by guest on 21 April 2026

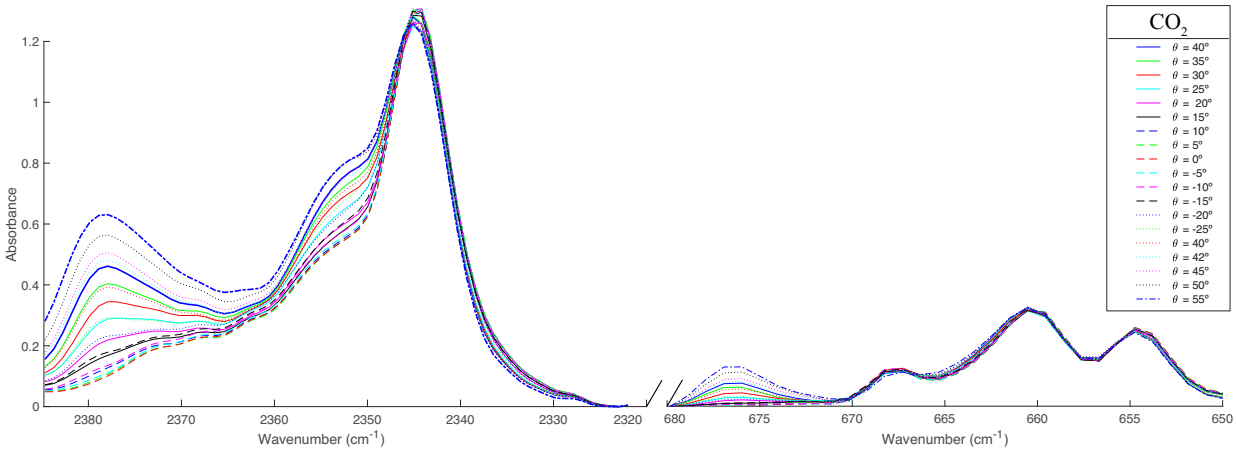


Figure 5. IR spectra of CO_2 ice deposited at 11 K measured at different incident angles.

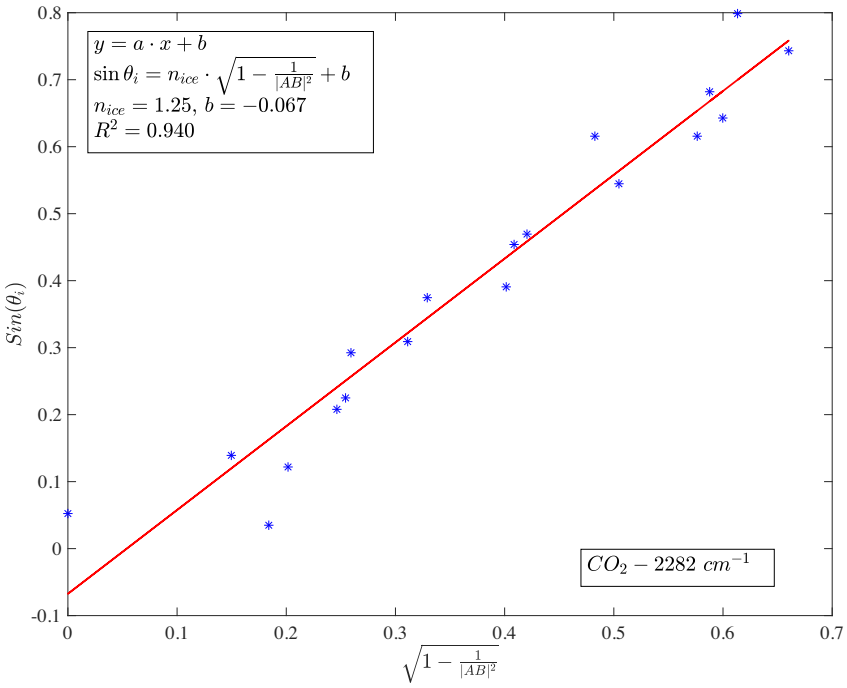


Figure 6. Representation of sine of incident angle of the IR beam, $\sin\theta_i$, for CO_2 ice deposited at 11 K as a function of $\sqrt{1-\frac{d^2}{|AB|^2}}$. Data corresponds to the band around 2282 cm^{-1}. The red-solid trace is the linear fit.

Using Snell's law,

$$n_{\rm vac}\sin\theta_i = n_{\rm ice}\sin\theta_t \tag{2}$$

we obtain

$$|AB| = \frac{d}{\cos(\arcsin\left(\frac{n_{\rm vac}\sin\theta_i}{n_{\rm ice}}\right)}. \tag{3}$$

If the medium surrounding the ice layer is air or vacuum, $n_{\rm vac} = 1$, equation (3) can be rearranged using $\cos(\arcsin x) = \sqrt{1-x^2}$ to obtain

$$|AB| = \frac{d\cdot n_{\rm ice}}{\sqrt{n_{\rm ice}^2 - \sin^2\theta_i}}. \tag{4}$$

Equation (4) can be expressed in its linear form $y = a\cdot x$

$$\sin\theta_i = n_{\rm ice}\cdot\sqrt{1-\frac{d^2}{|AB|^2}}, \tag{5}$$

where $y = \sin\theta_i$, $x = \sqrt{1-\frac{d^2}{|AB|^2}}$, and $a = n_{\rm ice}$ is the index of refraction of the ice that corresponds to the slope of the linear fit. If the data recorded by the FT-IR spectrometer is normalized, then $d = 1$.

Finally, in IR spectra acquired at incident angle θ_i, the correct value of the ice column density N_0 as if it were measured at normal incidence, can be easily obtained from the above equations:

$$N_0 = N_{\theta_i}\frac{|AB|_0}{|AB|_{\theta_i}} = N_{\theta_i}\sqrt{1-\frac{\sin^2\theta_i}{n_{\rm ice}^2}}. \tag{6}$$

Downloaded from https://academic.oup.com/mnras/article/538/3/1906/8043270 by guest on 21 April 2026

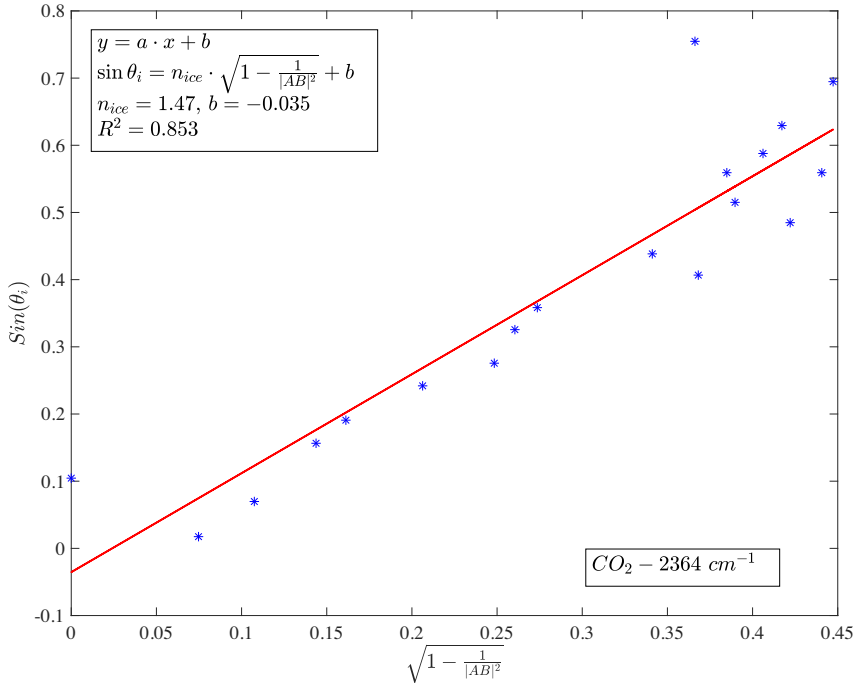


Figure 7. Representation of sine of incident angle of the IR beam, $\sin\theta_i$, for CO_2 ice deposited at 11 K as a function of $\sqrt{1 - \frac{d^2}{|AB|^2}}$. Data corresponds to the band around 2364 cm^{-1}. The red-solid trace is the linear fit.

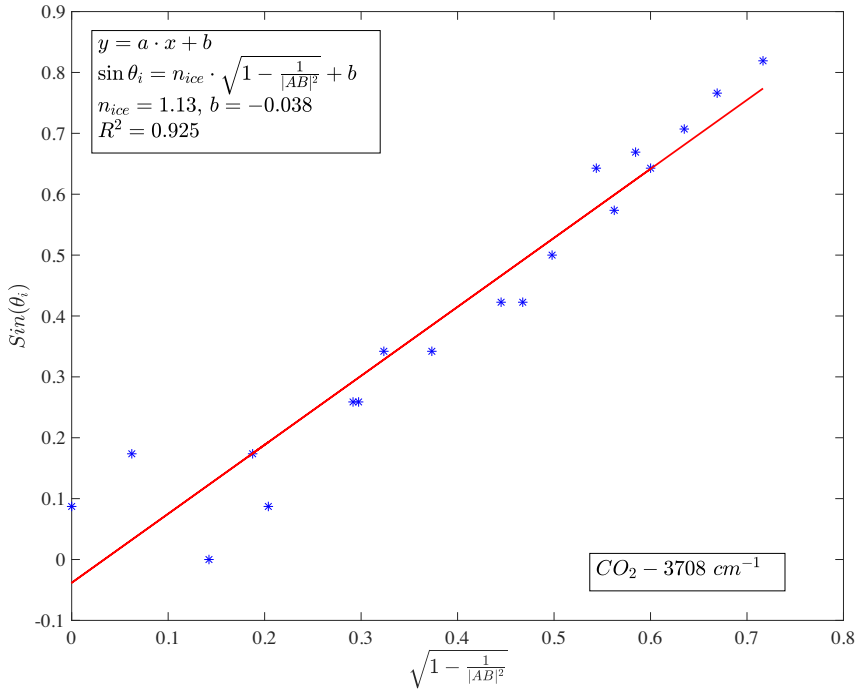


Figure 8. Representation of sine of incident angle of the IR beam, $\sin\theta_i$, for CO_2 ice deposited at 11 K as a function of $\sqrt{1 - \frac{d^2}{|AB|^2}}$. Data corresponds to the band around 3708 cm^{-1}. The red-solid trace is the linear fit.

Hence, equation (5) can be used to determine the absorption and column density at different incident angles. Additionally, from the slope of the linear fit, an *effective* refraction index, $n_{\rm ice}$, can be derived.

3 RESULTS

The spectroscopy performed at different incident angles of the more abundant ice components in interstellar ice mantles is presented as follows. First, the results are shown for the CO and CO_2 ices. These

Downloaded from https://academic.oup.com/mnras/article/538/3/1906/8043270 by guest on 21 April 2026

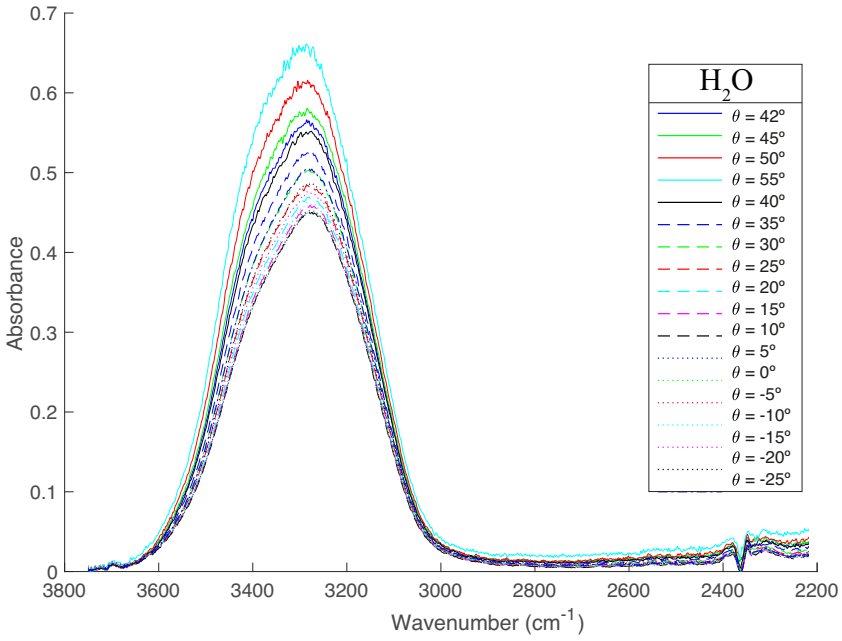


Figure 9. IR band around 3283 cm^{-1} of H_2O ice deposited at 11 K for various angles of incidence.

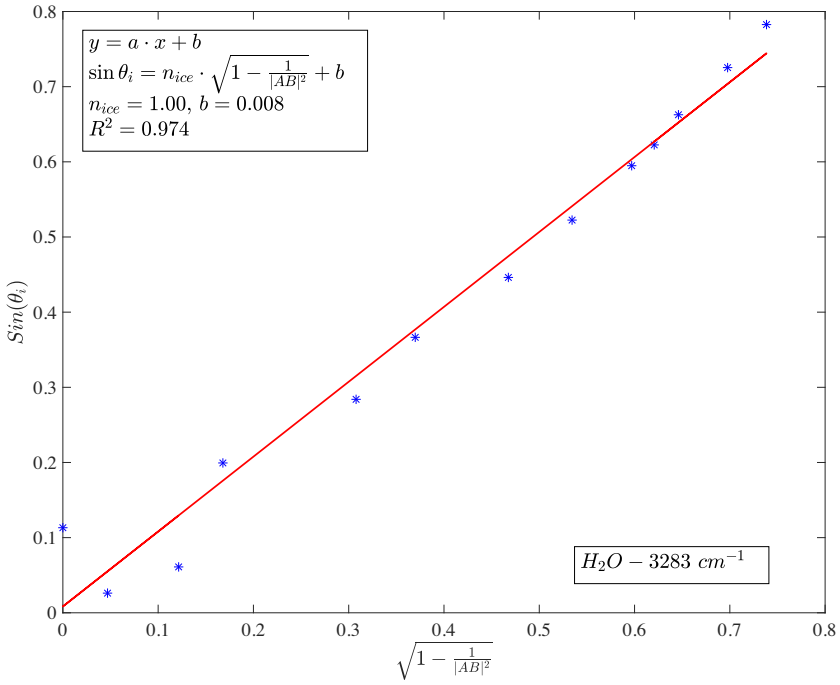


Figure 10. Representation of sine of incident angle of the IR beam, $\sin\theta_i$, for H_2O ice deposited at 11 K as a function of $\sqrt{1-\frac{d^2}{|AB|^2}}$. The red-solid trace is the linear fit.

ice samples exhibit clear effects related to the longitudinal (LO) and transverse (TO) optical modes when IR spectra are acquired at oblique incident angles. Second, H_2O, CH_3OH, NH_3, CH_4, and H_2S spectroscopy is presented. In general, these ice spectra only express the increase of the incident IR angle as an enhancement of the IR absorption bands. The growing IR absorption of these ices is simply explained by the larger IR beam path across the ice at oblique angles compared to normal incidence.

3.1 CO

As was mentioned in Section 1, the TO mode around 2138 cm^{-1} is the dominant one; see Fig. 2, while the LO mode around 2142 cm^{-1} gradually becomes observable as the incident angle increases up to about 40°, resembling a 'wing' of the TO mode at even larger angles. The appearance of the LO mode follows a slight blueshift of the IR band.

Downloaded from https://academic.oup.com/mnras/article/538/3/1906/8043270 by guest on 21 April 2026

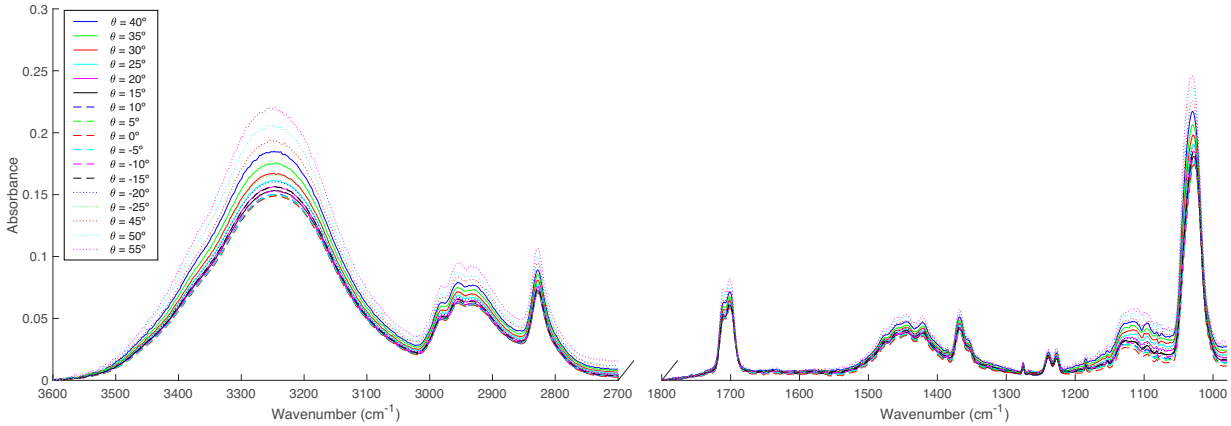


Figure 11. IR spectra of CH_3OH ice deposited at 11 K as a function of the incident angle used for IR spectrometry.

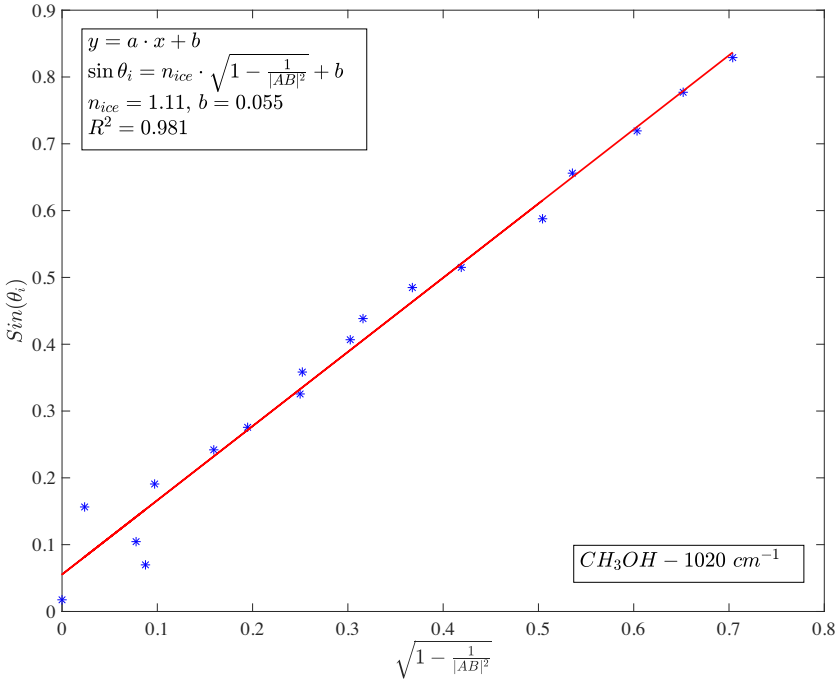


Figure 12. Representation of sine of incident angle of the IR beam, $\sin\theta_i$, for CH_3OH ice deposited at 11 K as a function of $\sqrt{1 - \frac{d^2}{|AB|^2}}$. Data corresponds to the band around 1020 cm^{-1}. The red-solid trace is the linear fit.

Fig. 3 illustrates the normalized values of the integrated IR absorption spectra of CO ice deposited at 11 K, plotted against the incident angle θ_i. Notably, as the incident angle increases, there is a corresponding increase in the normalized value of the integrated IR absorption. This phenomenon can be attributed to the increase of the IR path traversing through the deposited ice layer for oblique incident angles.

Fig. 4 shows $\sin\theta_i$ as a function of the $\sqrt{1 - \frac{d^2}{|AB|^2}}$ values with a linear fit. This fit provides a value of $n_{\rm ice} = 1.17$ which should be regarded as the *effective* index of refraction for CO ice deposited at 11 K in these experiments. This value of $n_{\rm ice}$ applies to the 2138 cm^{-1} band of CO and probably corresponds to an average value for the integrated absorption range of this band. The same holds for the other ice compositions reported here below. These $n_{\rm ice}$ values are provided in Table 1 and will be discussed in Section 4.

3.2 CO_2

Fig. 5 shows the IR spectra of pure CO_2 ice at different incident angles. The antisymmetric stretching fundamental ν_3 mode near 2343 cm^{-1} is little incident angle dependent, while the bands near 2351 cm^{-1} and 2380 cm^{-1} show an increasing absorption with the incident angle. The 2351 cm^{-1} band is related to the degree of porosity in the ice (Schiltz et al. 2024).

The 2380 cm^{-1} band corresponds to the longitudinal optical (LO) mode. It is often unnoticed in amorphous CO_2 ice spectra measured at normal incidence with an unpolarized IR beam (e.g. Falk 1987), and it is best observed in the crystalline ice form. However, this feature was observed using reflection-absorption IR spectroscopy for amorphous CO_2 deposited at 14 K with radiation polarized in the plane of propagation of the incident IR beam (P-polarized), indicating that the vibration of the 2380 cm^{-1} band is in the normal direction

Downloaded from https://academic.oup.com/mnras/article/538/3/1906/8043270 by guest on 21 April 2026

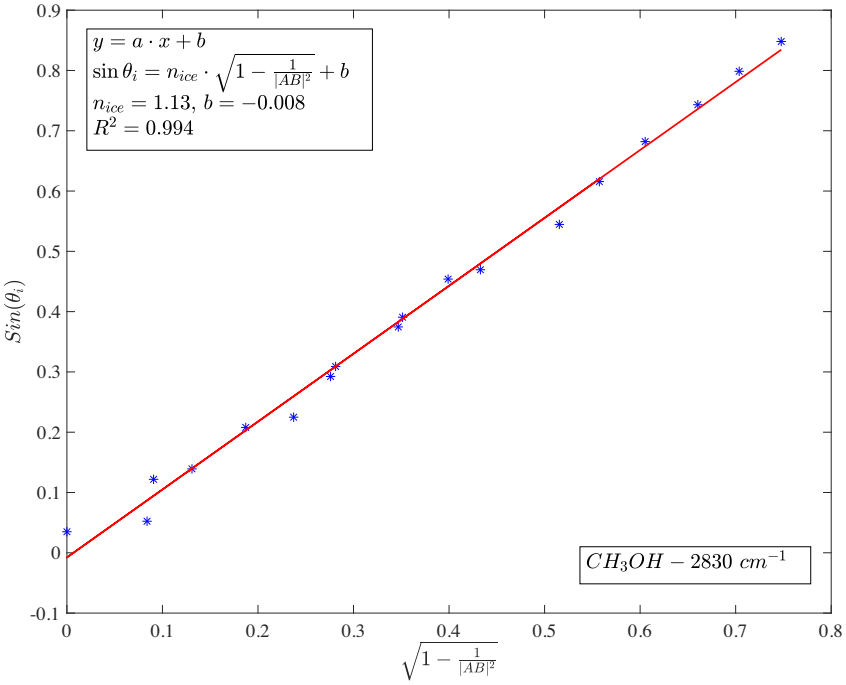


Figure 13. Representation of sine of incident angle of the IR beam, $\sin\theta_i$, for CH_3OH ice deposited at 11 K as a function of $\sqrt{1 - \frac{d^2}{|AB|^2}}$. Data corresponds to the band around 2830 cm^{-1}. The red-solid trace is the linear fit.

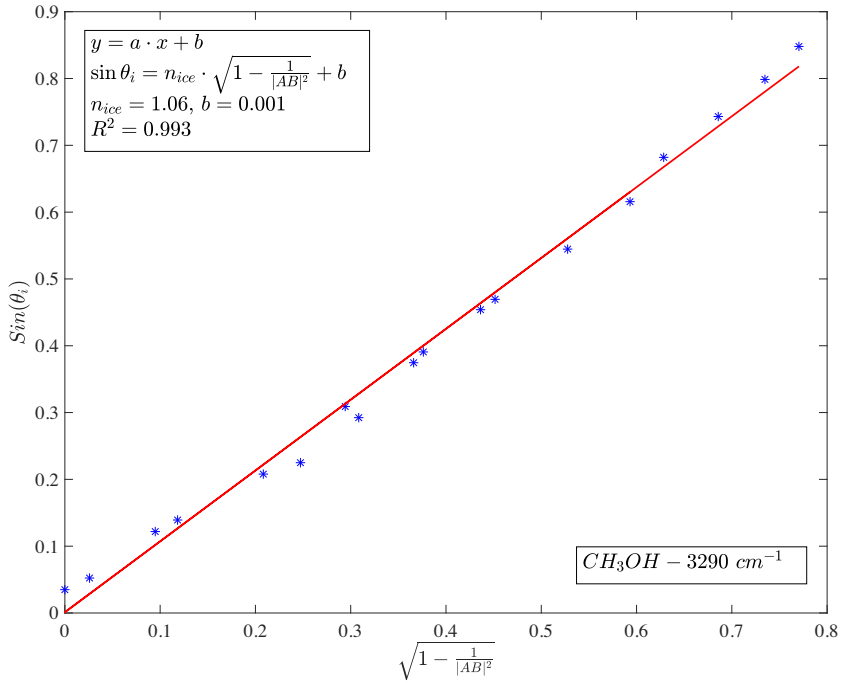


Figure 14. Representation of sine of incident angle of the IR beam, $\sin\theta_i$, for CH_3OH ice deposited at 11 K as a function of $\sqrt{1 - \frac{d^2}{|AB|^2}}$. Data corresponds to the band around 3290 cm^{-1}. The red-solid trace is the linear fit.

to the substrate or has vector components along that direction, as expected for the LO mode (Escribano et al. 2013). This orientation of the 2380 cm^{-1} band explains its increasing intensity for more oblique angles in Fig. 5. Escribano et al. (2013) explained that the CO_2 ice sample displays some crystalline character due to the layer accumulation (ice thickness increase) even at this low temperature, as evidenced by the splitting of the ν_2 (bending) modes. This argumentation is also valid for our experiments. Because the band around 2351 cm^{-1} follows the same trend as the 2380 cm^{-1} band, its corresponding vibration has a component in the direction normal to the ice surface. This preferred orientation, in addition to the association of this band with porosity in CO_2 ice, indicates

Downloaded from https://academic.oup.com/mnras/article/538/3/1906/8043270 by guest on 21 April 2026

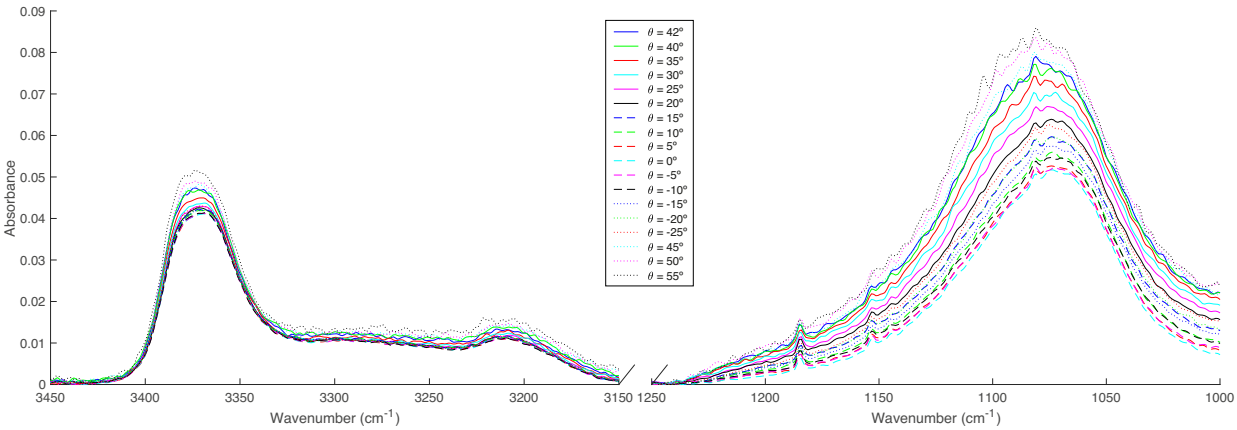


Figure 15. IR spectra of NH_3 ice deposited at 11 K as a function of the incident angle. The bands at 1082 cm^{-1} and 3375 cm^{-1} are displayed.

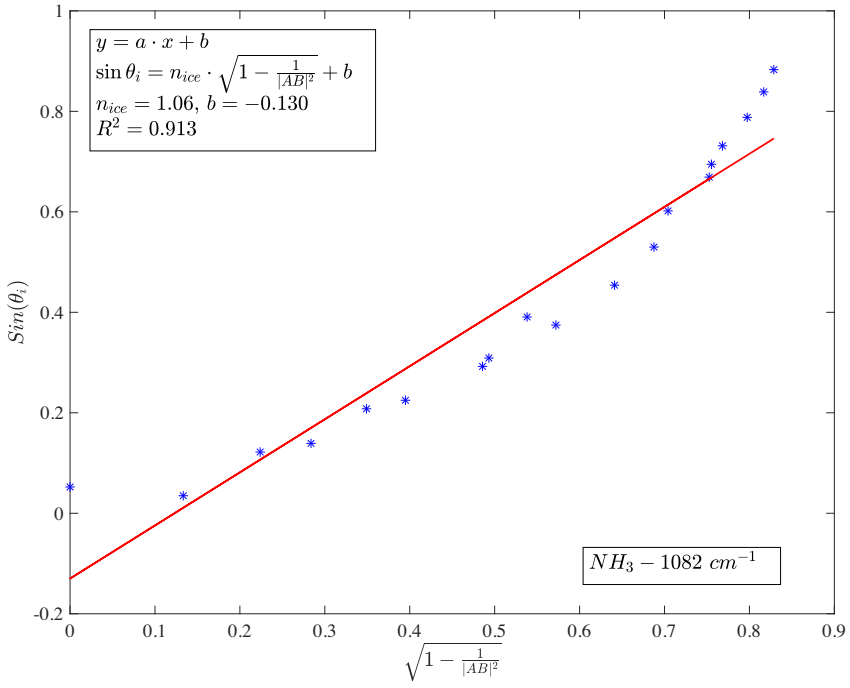


Figure 16. Representation of sine of incident angle of the IR beam, $\sin\theta_i$, for NH_3 ice deposited at 11 K as a function of $\sqrt{1 - \frac{d^2}{|AB|^2}}$. Data corresponds to the band around 1082 cm^{-1}. The red-solid trace is the linear fit.

that the plausible vibration is a dangling mode in CO_2 molecules (Schiltz et al. 2024). While danglings at the surface of the ice will follow the normal direction, danglings of molecules on pore walls may also be oriented differently with respect to the cold substrate. These danglings would account for the smaller absorption of the 2351 cm^{-1} band measured at normal incidence. As for the CO case, Fig. 7 shows the linear fit of the amorphous CO_2 ice spectral data that allows estimation of the *effective* index of refraction, $n_{CO_2} = 1.47$, for the 2364 cm^{-1} absorption. Figs 6 and 8 show the corresponding linear fits for the 2282 and 3708 cm^{-1} IR bands, respectively. The goodness of fit is acceptable, $R = 0.940$, 0.853, and 0.925, for the three bands.

3.3 H_2O

Fig. 9 shows the IR spectra of pure H_2O ice at different incident angles. It is observed that the increase in the angle of incidence is accompanied by an increasing absorbance. As already mentioned, this is due to the larger IR beam path going across the ice layer for increasing incident angles. The maximum absorbance occurs at the most oblique angle that could be measured in this experiment, 55°.

Fig. 10 shows $\sin\theta_i$ as a function of the $\sqrt{1 - \frac{d^2}{|AB|^2}}$ in H_2O ice spectra and the linear data fit. This data allows the estimation of the index of refraction, $n_{H_2O} = 1.00$. The goodness of fit is acceptable, $R = 0.974$. It should be regarded as the *effective* index of refraction

Downloaded from https://academic.oup.com/mnras/article/538/3/1906/8043270 by guest on 21 April 2026

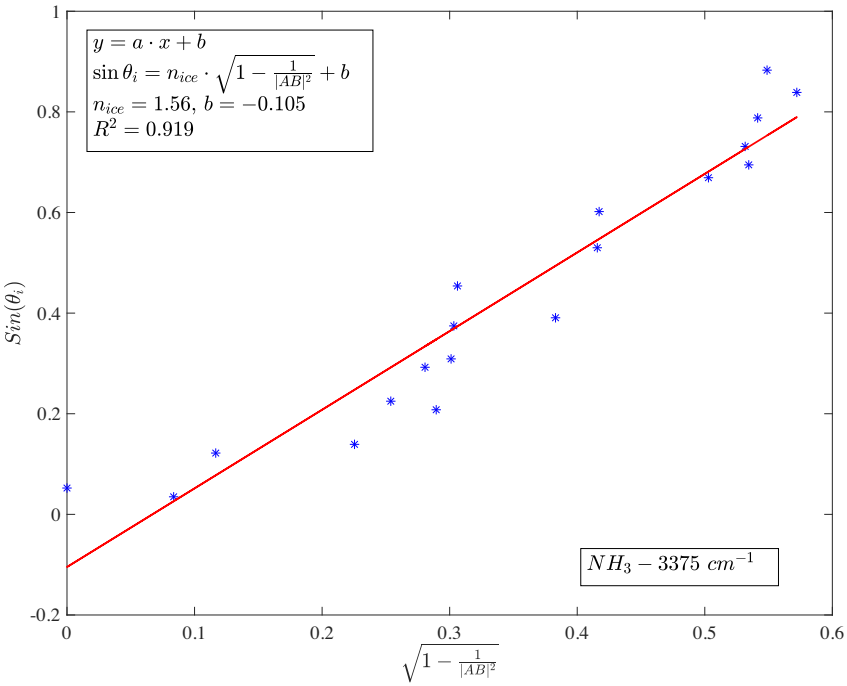


Figure 17. Representation of sine of incident angle of the IR beam, $\sin\theta_i$, for NH_3 ice deposited at 11 K as a function of $\sqrt{1 - \frac{d^2}{|AB|^2}}$. Data corresponds to the band around 3375 cm^{-1}. The red-solid trace is the linear fit.

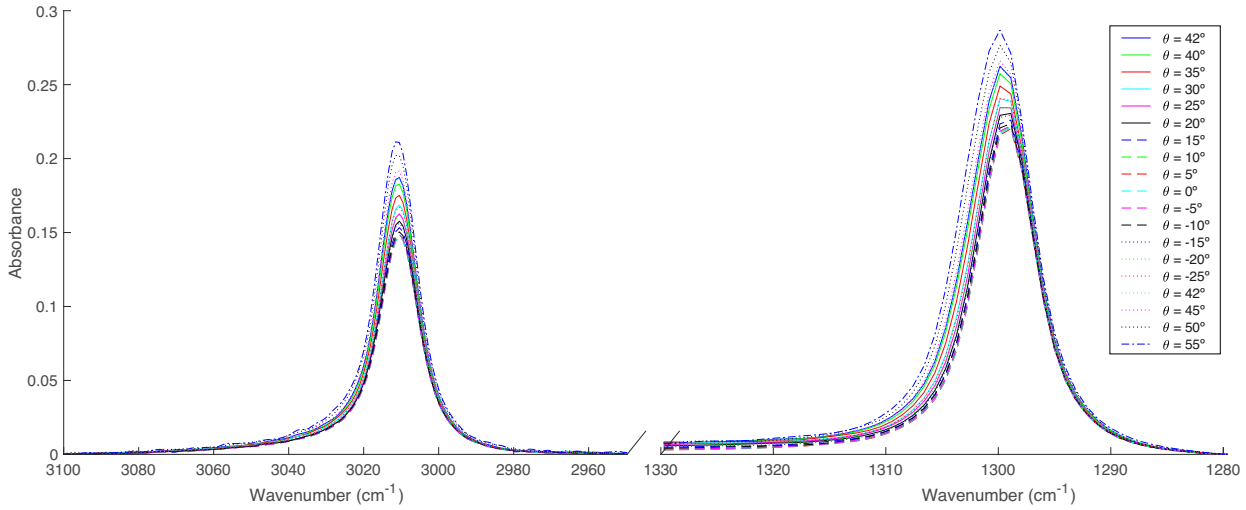


Figure 18. IR spectra of CH_4 ice deposited at 11 K, measured at different incident angles. The bands near 1300 cm^{-1} and 3010 cm^{-1} are displayed.

for H_2O ice deposited at 11 K in these experiments. This value applies to the 3283 cm^{-1} band of H_2O ice.

3.4 CH_3OH

Fig. 11 shows the IR spectra of CH_3OH ice at different incident angles. Figs 12, 13, and 14 display $\sin\theta_i$ as a function of the $\sqrt{1 - \frac{d^2}{|AB|^2}}$ for CH_3OH ice spectral data in the 1020, 2830, and 3290 cm^{-1} bands of CH_3OH, respectively. From these plots, the index of refraction was estimated, $n_{CH_3OH} = 1.11$, 1.13, and 1.06 for the 1020, 2830, and 3290 cm^{-1} bands of CH_3OH, respectively. The goodness of fit is acceptable, $R = 0.981$, 0.994, and 0.993. These values represent the *effective* index of refraction for CH_3OH ice deposited at 11 K in these experiments, which corresponds to an average value over the integrated absorption range of these bands.

3.5 NH_3

Fig. 15 shows the IR spectra of NH_3 ice at different incident angles. Figs 16 and 17 represent $\sin\theta_i$ as a function of the $\sqrt{1 - \frac{d^2}{|AB|^2}}$ for NH_3 ice spectral data in the 1082 and 3375 cm^{-1} bands of NH_3, respectively. From these plots, the index of refraction are estimated,

Downloaded from https://academic.oup.com/mnras/article/538/3/1906/8043270 by guest on 21 April 2026

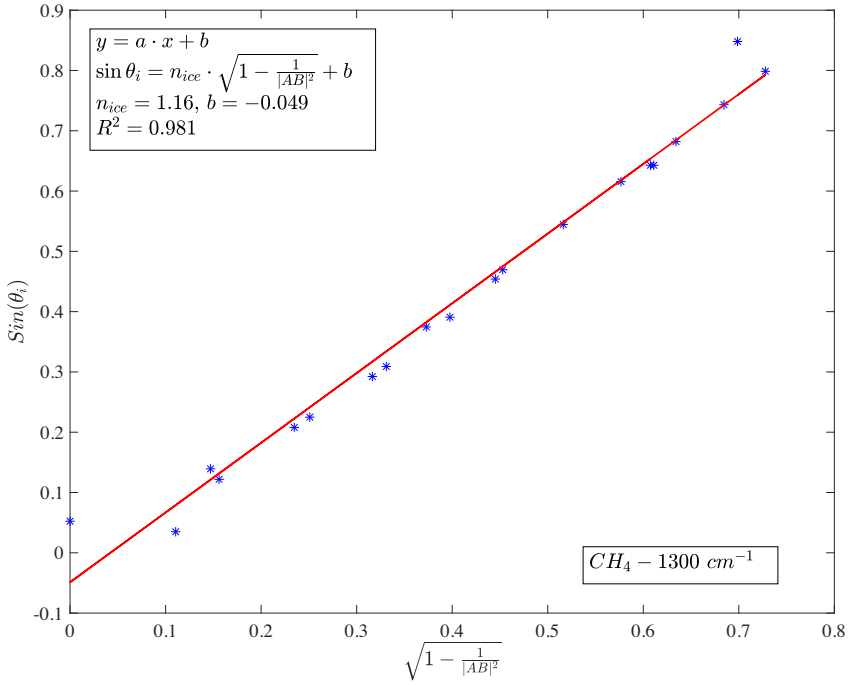


Figure 19. Representation of sine of incident angle of the IR beam, $\sin\theta_i$, for CH_4 ice deposited at 11 K as a function of $\sqrt{1 - \frac{d^2}{|AB|^2}}$. Data corresponds to the band around 1300 cm^{-1}. The red-solid trace is the linear fit.

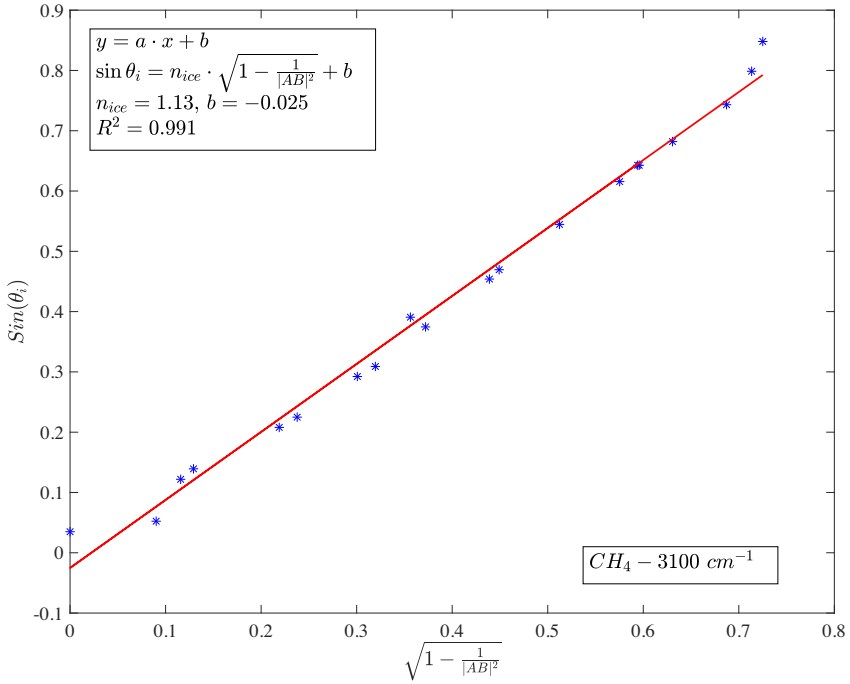


Figure 20. Representation of sine of incident angle of the IR beam, $\sin\theta_i$, for CH_4 ice deposited at 11 K as a function of $\sqrt{1 - \frac{d^2}{|AB|^2}}$. Data corresponds to the band around 3100 cm^{-1}. The red-solid trace is the linear fit.

$n_{NH_3} = 1.06$ and 1.56 for the 1082 and 3375 cm^{-1} band of NH_3. The goodness of fit is acceptable, $R = 0.913$ and 0.919. These values represent the *effective* refractive index for NH_3 ice deposited at 11 K in these experiments.

3.6 CH_4

Fig. 18 shows the IR spectra of CH_4 ice at different incident angles. Figs 19 and 20 display $\sin\theta_i$ as a function of the $\sqrt{1 - \frac{d^2}{|AB|^2}}$ for CH_4 ice spectra in the 1300 and 3100 cm^{-1} bands. From these

Downloaded from https://academic.oup.com/mnras/article/538/3/1906/8043270 by guest on 21 April 2026

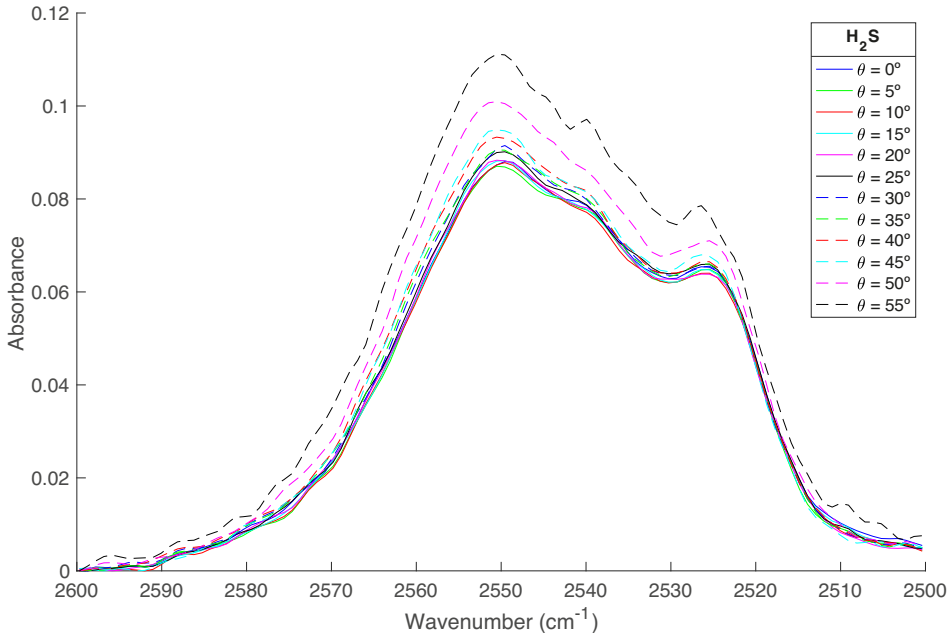


Figure 21. IR band near 2550 cm^{-1} of H_2S ice deposited at 11 K as a function of incident angle.

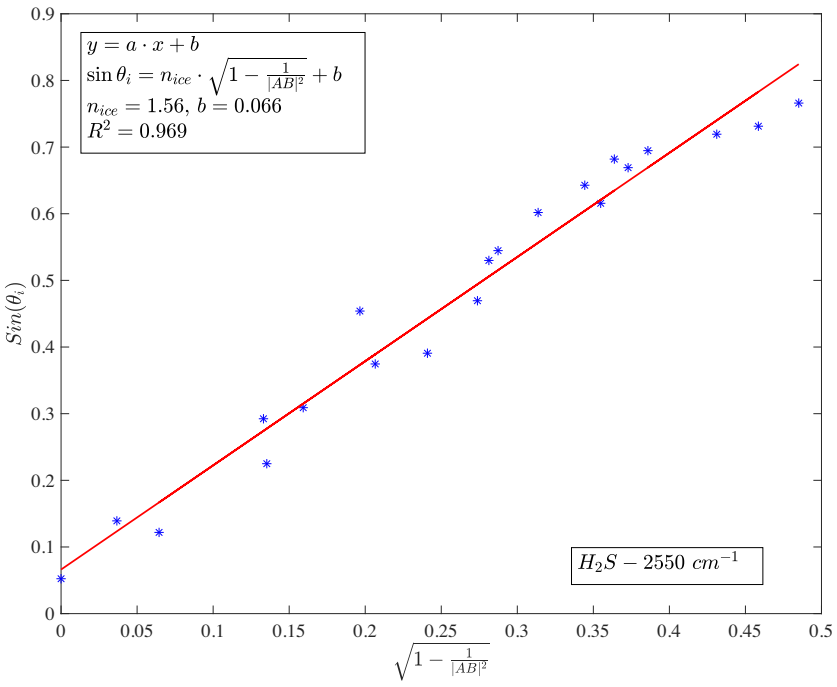


Figure 22. Representation of sine of incident angle of the IR beam, $\sin\theta_i$, for H_2S ice deposited at 11 K as a function of $\sqrt{1-\frac{d^2}{|AB|^2}}$. Data corresponds to the band around 2550 cm^{-1}. The red-solid trace is the linear fit.

plots, the index of refraction are estimated, $n_{CH_4} = 1.16$ and 1.13 for the 1300 and 3100 cm^{-1} band of CH_4, respectively. The corresponding goodness-of-fit values are $R = 0.981$ and 0.991. These values represent the *effective* refractive index for CH_4 ice deposited at 11 K.

3.7 H_2S

Fig. 21 shows the IR spectra of H_2S ice at different incident angles. The increase in the angle of incidence that corresponds to a larger optical path across the ice layer, is accompanied by an increase in the IR absorbance.

Downloaded from https://academic.oup.com/mnras/article/538/3/1906/8043270 by guest on 21 April 2026

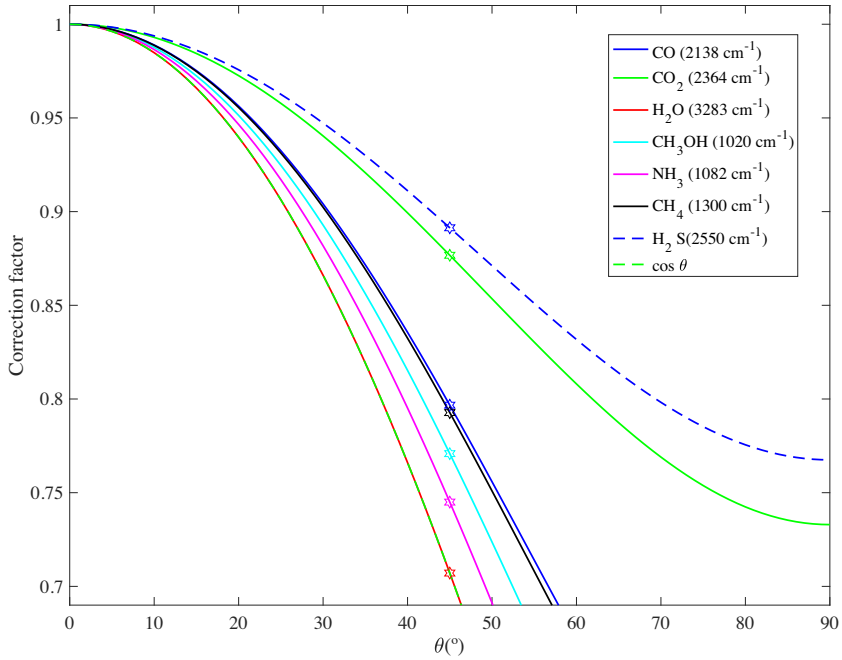


Figure 23. Representation of the correction factor $\sqrt{1-\frac{\sin^2\theta_i}{n_{\rm ice}^2}}$ in equation (6) for different incident angle θ_i values of the IR beam with respect to the ice substrate.

Fig. 22 presents $\sin\theta_i$ as a function of the $\sqrt{1-\frac{d^2}{|AB|^2}}$ in the acquired H_2S ice spectra and the linear fit of the data. The estimated index of refraction is $n_{H_2S} = 1.56$ with a goodness of fit of $R = 0.969$. As in the previous sections, this should be regarded as the *effective* index of refraction for H_2S ice deposited at 11 K. This value applies to the 2550 cm^{-1} band of H_2S.

4 CONCLUSIONS AND ASTROPHYSICAL IMPLICATIONS

The *effective* index of refraction $n_{\rm ice}$ obtained in this work corresponds to an average value in the spectral range used for the integration of the IR bands. The effective refractive index values presented in Table 1 are close to the average value of the refraction index n in the spectral range where these absorption bands are located. It should be noted that the values of $n_{\rm ice}$ in Table 1 are obtained in the IR. The reader may be more used to the ice values measured in the optical range since they are used to obtain the ice thickness using visible laser interferometry (e.g. Luna et al. 2022; González Díaz et al. 2022). The values of the correction factor $\sqrt{1-\frac{\sin^2\theta_i}{n_{\rm ice}^2}}$ in equation (6) for $\theta_i = 45^\circ$ are also presented in Table 1, since this is a commonly used angle in astrochemistry laboratories that perform IR spectroscopy of astrophysical ice analogues. Finally, Fig. 23 is a representation of this correction factor as a function of the incident angle for the various ice compositions studied in this work.

This paper allows to estimate the correct value of the column density of astrophysically relevant ice components when IR spectroscopy is performed at oblique incidence with respect to the ice sample. More oblique incident angles lead to an increase in the optical path of the IR beam across the ice, which is also dependent on the index of refraction of the ice. As a result, the IR absorption increases with increasing incident angle. In addition, the cases of CO and CO_2 ice show the important effect of LO and TO modes on the IR absorption bands, since oblique incident angles intercept both modes. This effect was used to infer information on the ice structure. For instance, a more ordered or crystalline ice structure can be identified because the alignment and orientation of the molecules is reflected in the distribution of LO and TO modes.

The results presented here concern ice layers made of a pure ice component deposited at 11 K. The effect of deposition temperature on the spectroscopy at oblique angles is left for future work. The astrophysical scenario of ice spectroscopy, where the ice mantle build up may take place at an extended temperature range, is much more complex. This ice mantle on top of dust grains will adapt to the morphology of the bare grain surface, which is expected to deviate from a flat surface, and the IR photons will impinge on the ice at different angles. Among other effects, micron-size ice-covered dust grains intercepted along the line of sight suffer from scattering effects at mid-IR wavelengths, this has a considerable impact on the IR band profiles of the ice (Dartois et al. 2024). Furthermore, the interaction of different molecular species in the ice, either with the dominant water ice matrix or among less abundant species, leads to band deformations and wavenumber shifts, or even the formation of new bands that are not present in the pure ice components (Martín-Doménech et al. 2014).

ACKNOWLEDGEMENTS

This research has been funded by project PID2020-118974GB-C21 by the Spanish Ministry of Science and Innovation.

DATA AVAILABILITY

The data underlying this article will be shared on reasonable request to the corresponding author.

Downloaded from https://academic.oup.com/mnras/article/538/3/1906/8043270 by guest on 21 April 2026

REFERENCES

Dartois E. et al., 2024, Nat. Astron., 8, 359

Escribano R. M., Munoz Caro G. M., Cruz-Diaz G. A., Rodriguez-Lazcano Y., Mate B., 2013, Proc. Natl. Acad. Sci., 110, 12899

Falk M., 1987, J. Chem. Phys., 86, 560

González Díaz C., Carrascosa H., Muñoz Caro G. M., Satorre M. Á., Chen Y.-J., 2022, MNRAS, 517, 5744

González Díaz C., Carrascosa de Lucas H., Aparicio S., Muñoz Caro G. M., Sie N.-E., Hsiao L.-C., Cazaux S., Chen Y.-J., 2019, MNRAS, 486, 5519

Itoh Y., Kasuya A., Hasegawa T., 2009, J. Phys. Chem. A, 113, 7810

Lasne J., Rosu-Finsen A., Cassidy A., McCoustra M. R. S., Field D., 2015, Phys. Chem. Chem. Phys., 17, 30177

Luna R., Millán C., Domingo M., Santonja C., Satorre M. Á., 2022, ApJ, 935, 134

Martín-Doménech R., Muñoz Caro G. M., Bueno J., Goesmann F., 2014, A&A, 564, A8

Muñoz Caro G. M., Jiménez-Escobar A., Martín-Gago J. Á., Rogero C., Atienza C., Puertas S., Sobrado J. M., Torres-Redondo J., 2010, A&A, 522, A108

Muñoz Caro G. M., Chen Y.-J., Aparicio S., Jiménez-Escobar A., Rosu-Finsen A., Lasne J., McCoustra M. R. S., 2016, A&A, 589, A19

Öberg K. I., Facchini S., Anderson D. E., 2023, ARA&A, 61, 287

Palumbo M. E., 2006, A&A, 453, 903

Schiltz L. et al., 2024, A&A, 688, A155

Zumofen G., 1978, J. Chem. Phys., 68, 3747

This paper has been typeset from a TEX/LATEX file prepared by the author.

Downloaded from https://academic.oup.com/mnras/article/538/3/1906/8043270 by guest on 21 April 2026

© 2025 The Author(s).
Published by Oxford University Press on behalf of Royal Astronomical Society. This is an Open Access article distributed under the terms of the Creative Commons Attribution License (https://creativecommons.org/licenses/by/4.0/), which permits unrestricted reuse, distribution, and reproduction in any medium, provided the original work is properly cited.